charge transfer states. In particular, it has been demonstrated that inertial solvation dynamics likely play a key role in the process of charge localization after photo-induced charge transfer. It is unclear to what extent these results can be extended to other, more complex chemical and biological systems. However, given the desirability for vectorial charge transport in various contexts, we believe that medium-induced localization dynamics may be important in a wide range of settings.

References and Notes

1. D. O. Hall and K. K. Rao, Eds., *Photosynthesis* (Cambridge Univ. Press, New York, ed. 5, 1995).
2. S. K. Deb, *Curr. Opin. Solid State Mater. Sci.* **3**, 51 (1998).
3. G. A. Voth and R. M. Hochstrasser, *J. Phys. Chem.* **100**, 13034 (1996).
4. R. M. Stratt and M. Maroncelli, *J. Phys. Chem.* **100**, 12981 (1996).
5. M. Maroncelli, *J. Mol. Liq.* **57**, 1 (1993).
6. G. R. Fleming and M. H. Cho, *Annu. Rev. Phys. Chem.* **47**, 109 (1996).
7. C. J. Cramer and D. G. Truhlar, *Chem. Rev.* **99**, 2161 (1999).
8. F. O. Raineri and H. L. Friedman, *Adv. Chem. Phys.* **107**, 81 (1999).
9. V. Balzani, A. Juris, M. Venturi, S. Campagna, S. Serroni, *Chem. Rev.* **96**, 759 (1996), and references therein.
10. K. Kalyanasundaram and M. Grätzel, *Coord. Chem. Rev.* **177**, 347 (1998).
11. J. N. Demas and G. A. Crosby, *J. Am. Chem. Soc.* **93**, 2841 (1971).
12. J. N. Demas and D. G. Taylor, *Inorg. Chem.* **18**, 3177 (1979).
13. H. Yersin, W. Humbs, J. Strasser, *Coord. Chem. Rev.* **159**, 325 (1997), and references therein.
14. D. Braun, E. Gallhuber, H. Yersin, *Chem. Phys. Lett.* **171**, 122 (1990).
15. D. Braun, P. Huber, J. Wudy, J. Schmidt, H. Yersin, *J. Phys. Chem.* **98**, 8044 (1994).
16. H. Riesen, L. Wallace, E. Krausz, *Inorg. Chem.* **35**, 6908 (1996).
17. J. S. Gold, S. J. Milder, J. W. Lewis, D. S. Kliger, *J. Am. Chem. Soc.* **107**, 8285 (1985).
18. E. M. Kober, B. P. Sullivan, T. J. Meyer, *Inorg. Chem.* **23**, 2098 (1984).
19. D. H. Oh, M. Sano, S. G. Boxer, *J. Am. Chem. Soc.* **113**, 6880 (1991), and references therein.
20. P. J. Carroll and L. E. Brus, *J. Am. Chem. Soc.* **109**, 7613 (1987).
21. P. G. Bradley, N. Kress, B. A. Hornberger, R. F. Dallinger, W. H. Woodruff, *J. Am. Chem. Soc.* **103**, 7441 (1981).
22. M. Forster and R. E. Hester, *Chem. Phys. Lett.* **81**, 42 (1981).
23. L. F. Cooley, P. Bergquist, D. F. Kelley, *J. Am. Chem. Soc.* **112**, 2612 (1990).
24. R. A. Malone and D. F. Kelley, *J. Chem. Phys.* **95**, 8970 (1991).
25. T. Yabe *et al.*, *J. Phys. Chem.* **94**, 7128 (1990).
26. N. H. Damrauer *et al.*, *Science* **275**, 54 (1997).
27. R. G. Gordon, *J. Chem. Phys.* **45**, 1643 (1966).
28. D. M. Jonas, M. J. Lang, Y. Nagasawa, T. Joo, G. R. Fleming, *J. Phys. Chem.* **100**, 12660 (1996).
29. R. W. Schoenlein, J.-Y. Bigot, M. T. Portella, C. V. Shank, *Appl. Phys. Lett.* **58**, 801 (1991).
30. The pulses used for the time-resolved anisotropy measurements were 25 fs in duration centered at 480 nm at a repetition rate of 540 Hz. The polarization of the probe beam was oriented 45° to the pump. After the beams were crossed in the sample, the probe was split by a polarization beam-splitting cube to facilitate simultaneous detection of polarization components parallel and perpendicular to the pump. The measured anisotropies were calibrated with control experiments on laser dye samples that yielded values of $r = 0.4$ for nondegenerate transition dipoles.
31. C. Daul, E. J. Baerends, P. Vernooijs, *Inorg. Chem.* **33**, 3538 (1994).
32. Values for $r(t)$ were found to be independent of probe wavelength in the range of 465 to 500 nm on the basis of anisotropy data reconstructed from polarized full spectra.
33. Rotational depolarization of this molecule occurs on the time scale of several tens of ps in fluid solution [cf. (*23*)].
34. N. Sutin and C. Creutz, *Adv. Chem. Ser.* **168**, 1 (1978); B. T. Weldon and J. K. McCusker, in preparation.
35. H. Hiratsuka, K. Sekiguchi, Y. Hatano, Y. Tanizaki, Y. Mori, *Can. J. Chem.* **65**, 1185 (1987).
36. This calculation assumes random selection of the three possible MLCT transition dipoles; thus, $r_\alpha = 0.1$. In addition, we do not observe stimulated emission from this compound ($\gamma = 0$).
37. Time dependence of the anisotropy arising from spectral shifting is considered to be unlikely because of the probe wavelength independence of $r(t)$ [cf. (*32*)].
38. C. Galli, K. Wynne, S. M. LeCours, M. J. Therien, R. M. Hochstrasser, *Chem. Phys. Lett.* **206**, 493 (1993).
39. K. Wynne and R. M. Hochstrasser, *Chem. Phys.* **171**, 179 (1993).
40. A value of $r(0)$ between 1.52 and 0.22 is to be expected if the electronic dephasing time is substantially (though not infinitely) shorter than the excitation pulse. Values of $r(0) \sim 0.6$ (Table 1) are therefore consistent with partial dephasing in $[Ru(bpy)_3]^{2+}$ within the ~25-fs excitation pulse.
41. A similar model has been suggested by other workers on the basis of static variable-temperature emission spectra. See J. Ferguson and E. R. Krausz, *J. Phys. Chem.* **91**, 3161 (1987), and references therein.
42. S. A. Passino, Y. Nagasawa, G. R. Fleming, *J. Chem. Phys.* **107**, 6094 (1997), and references therein.
43. A 25-fs pump pulse centered at 480 nm and a 10-fs broadband probe were used for the transient absorption measurements. After the pump and probe were crossed in the sample, the broadband probe was coupled into an optical multichannel analyzer for spectral measurements.
44. C. H. Brito Cruz, R. L. Fork, C. V. Shank, *Opt. Lett.* **12**, 483 (1987).
45. We thank G. Fleming for helpful discussions. This research was supported by the Director, Office of Science, Office of Basic Energy Sciences of the U.S. Department of Energy grant DE-FG03-96ER14665 (J.K.M.) and contract DE-AC03-76F00098 (C.V.S.).

20 March 2000; accepted 14 June 2000

O_2 Activation by Nonheme Iron Complexes: A Monomeric Fe(III)–Oxo Complex Derived From O_2

Cora E. MacBeth,[1] Adina P. Golombek,[3] Victor G. Young Jr.,[4] Cheng Yang,[1] Krzysztof Kuczera,[1,2] Michael P. Hendrich,[3] A. S. Borovik[1]*

Iron species with terminal oxo ligands are implicated as key intermediates in several synthetic and biochemical catalytic cycles. However, there is a dearth of structural information regarding these types of complexes because their instability has precluded isolation under ambient conditions. The isolation and structural characterization of an iron(III) complex with a terminal oxo ligand, derived directly from dioxygen (O_2), is reported. A stable structure resulted from placing the oxoiron unit within a synthetic cavity lined with hydrogen-bonding groups. The cavity creates a microenvironment around the iron center that aids in regulating O_2 activation and stabilizing the oxoiron unit. These cavities share properties with the active sites of metalloproteins, where function is correlated strongly with site structure.

The activation of O_2 by Fe(II) complexes is of fundamental importance in biology. Heme and nonheme iron enzymes use O_2 as the primary oxidant in various biochemical transformations (*1–3*). In many of these enzymes, iron species with terminal oxo ligands are proposed as key intermediates in the catalytic cycle. Spectroscopic and structural (*4*, *5*) results are consistent with these species being high valent iron centers having formal oxidation states of $\geq 4+$. In synthetic porphyrin systems, spectroscopic and mechanistic evidence suggests that these oxoiron species can be generated at temperatures $< -40°C$ (*6*), but these complexes have yet to be structurally characterized by x-ray diffraction (XRD) methods. There is considerably less information on synthetic nonheme iron species with terminal oxo ligands—their existence is often inferred from mechanistic considerations alone (*7*, *8*). Efforts to model mononuclear heme and nonheme oxoiron species derived from O_2 are hindered by the strong thermodynamic preference of Fe(III) complexes to form μ-oxo bridged diiron species, Fe(III)-$(O)_n$-Fe(III) (*9*).

Metalloproteins overcome these obstacles

---

[1] Department of Chemistry and [2] Department of Molecular Biosciences, University of Kansas, Lawrence, KS 66045, USA. [3] Department of Chemistry, Carnegie-Mellon University, Pittsburgh, PA 15213, USA. [4] Department of Chemistry, University of Minnesota, Minneapolis, MN 55455, USA.

*To whom correspondence should be addressed.

by using microenvironmental effects within their active sites to influence function (*10*, *11*). Noncovalent interactions, such as hydrogen bonds (H-bonds), are instrumental in regulating chemical processes, including those observed in respiratory proteins (*12*) and metal-containing hydrolases (*13*). Recent XRD studies (2.2 Å resolution) on compound I of cytochrome c peroxidase show that H-bonding occurs between an active-site arginine (Arg^{48}) and the Fe(IV)=O center (*4*). Spectroscopic measurements on compound II of horseradish peroxidase (*14*) and theoretical studies of models for bleomycin (*15*) further suggest that activity is partially regulated by H-bonding to oxoiron units. We have used these principles of molecular design to develop synthetic systems that regulate structure and function around metal ions by creating biomimetic microenvironments (*16*, *17*). The tripodal ligand tris[(*N*′-*tert*-butylureaylato)-*N*-ethyl)]aminato ($[H_3\mathbf{1}]^{3-}$) can stabilize monomeric M–O and M–OH complexes by forming a H-bonding cavity around vacant coordination sites when bonded to a metal ion (*16*–*22*). Reported herein is the formation, structure, and properties of $[Fe(III)H_3\mathbf{1}(O)]^{2-}$, a mononuclear oxoiron complex in which the terminal oxo ligand is derived directly from dioxygen (*23*). Also presented are the properties of the Fe(III)–OH and Fe(II)–OH analogs, $[Fe(III)H_3\mathbf{1}(OH)]^{1-}$ and $[Fe(II)H_3\mathbf{1}(OH)]^{2-}$.

The syntheses of $[Fe(III)H_3\mathbf{1}(O)]^{2-}$ and $[Fe(III)H_3\mathbf{1}(OH)]^{1-}$ are outlined in Fig. 1 (*24*). Both Fe(III) complexes were generated from Fe(II) precursors and 0.5 equivalents (equiv) of O_2 dissolved in dimethylacetamide (DMA). The formation of these complexes depends on the amount of base used during the initial deprotonation of $H_6\mathbf{1}$. $[Fe(III)H_3\mathbf{1}(O)]^{2-}$ was isolated after crystallization in 50% overall yield when 4 equiv of KH was used. In contrast, the use of 3 equiv of KH affords $[Fe(III)H_3\mathbf{1}(OH)]^{1-}$ as the major product (55% yield). When these reactions were performed in the presence of 9,10-dihydroanthracene (*25*–*27*), $[Fe(III)H_3\mathbf{1}(O)]^{2-}$ and $[Fe(III)H_3\mathbf{1}(OH)]^{1-}$ were produced in crystalline yields of 62 and 90%, with concomitant formation of anthracene in ~90% isolated yield. Moreover, $[Fe(III)H_3\mathbf{1}(O)]^{2-}$ was converted to $[Fe(III)H_3\mathbf{1}(OH)]^{1-}$ in the presence of 1 equiv of H_2O and to $[Fe(III)H_3\mathbf{1}(OMe)]^{1-}$ when treated with 1 equiv of methyl iodide.

The formation of the oxo ligand in $[Fe(III)H_3\mathbf{1}(O)]^{2-}$ from O_2 was confirmed by labeling studies. We synthesized the Fe(III)–^{18}O complex following the procedure shown in Fig. 1 using $^{18}O_2$. The $\nu(Fe^{16}O)$ band appears at 671 cm^{-1} in the Fourier transform infrared (FTIR) spectrum of $[Fe(III)H_3\mathbf{1}(^{16}O)]^{2-}$. This band shifts to 645 cm^{-1} in $[Fe(III)H_3\mathbf{1}(^{18}O)]^{2-}$ [FTIR: $\nu(Fe^{16}O)/\nu(Fe^{18}O) = 1.05$; calculated (calcd.) 1.05]. Moreover, the O atom of the OH group in $[Fe(III)H_3\mathbf{1}(OH)]^{1-}$ also originates from O_2. $[Fe(III)H_3\mathbf{1}(^{16}OH)]^{1-}$ displays a $\nu(^{16}OH) = 3632\ cm^{-1}$, which shifts to 3621 cm^{-1} in $[Fe(III)H_3\mathbf{1}(^{18}OH)]^{1-}$ [FTIR: $\nu(^{16}OH)/\nu(^{18}OH) = 1.003$; calcd. 1.004]. The $\nu(OH)$ band is absent in $[Fe(III)H_3\mathbf{1}(O)]^{2-}$.

A proposed mechanism consistent with these observations involves a dinuclear peroxo-bridged species (Fig. 2). Homolysis of the O–O bond produces an oxoiron(IV) intermediate whose oxo moiety is sufficiently buried inside the cavity to prevent reactions with other hindered iron centers. This oxoiron(IV) species is competent to abstract H· from external reagents (such as solvent or 9,10-dihydroanthracene) to produce Fe(III)–OH complexes. $[Fe(III)H_2\mathbf{1}(OH)]^{2-}$ is formed when 4 equiv of base are used in the reaction (Fig. 2). This complex has a basic ureaylate group within the cavity, disposed near the coordinated hydroxo ligand. Intramolecular proton transfer between this basic site and Fe-OH unit is likely and results in the observed Fe(III)–oxo product, $[Fe(III)H_3\mathbf{1}(O)]^{2-}$. In the absence of this basic site within the cavity, as occurs when only 3 equiv of KH are used in the reaction, $[Fe(III)H_3\mathbf{1}(OH)]^{1-}$ is the major product.

The monomeric character of $[Fe(III)H_3\mathbf{1}(O)]^{2-}$ was established by an XRD study (*24*). The $K_2[Fe(III)H_3\mathbf{1}(O)]$ salt crystallized with two independent, but nearly identical, anions ($[Fe(III)H_3\mathbf{1}\text{-}\mathbf{a}(O)]^{2-}$ and $[Fe(III)H_3\mathbf{1}\text{-}\mathbf{b}(O)]^{2-}$) in the asymmetric unit. These two anions have a trigonal bipyramidal coordination geometry around the Fe(III) centers, as shown in Fig. 3 for $[Fe(III)H_3\mathbf{1}\text{-}\mathbf{b}(O)]^{2-}$ (*28*). In both complexes, the trigonal plane is formed by three urea nitrogens from $[H_3\mathbf{1}]^{3-}$ with an average Fe–N_{urea} distance of 2.056 ± 0.002 Å. The oxo oxygen is positioned trans to the apical nitrogen in each complex with an Fe1–O_{oxo} distance of 1.813 ± 0.003 Å. These distances are similar to those found in complexes with Fe(III)–O–Fe(III) cores (*9*) but are 0.147 Å longer than those found in $[FeO_4]^{2-}$, an Fe(VI) complex that is the only other structurally characterized iron complex with terminal oxo ligands (*29*). Spectroscopic

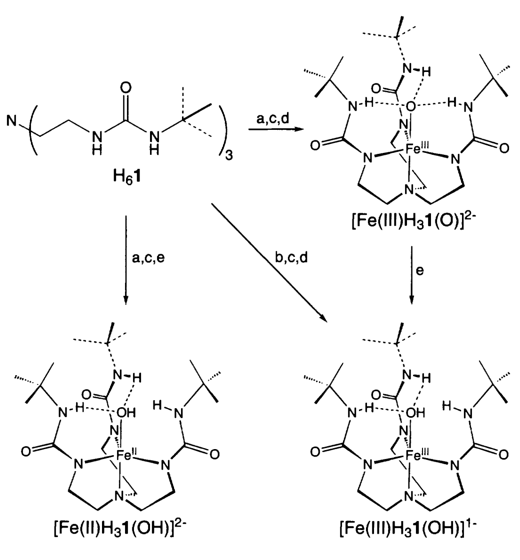

Fig. 1. Conditions: a, 4 equiv KH, DMA, inert atmosphere (Ar), room temperature; b, 3 equiv KH, DMA, Ar, room temperature; c, $Fe(OAc)_2$, DMA, Ar, room temperature; d, 0.5 equiv O_2, DMA, room temperature; e, H_2O, room temperature.

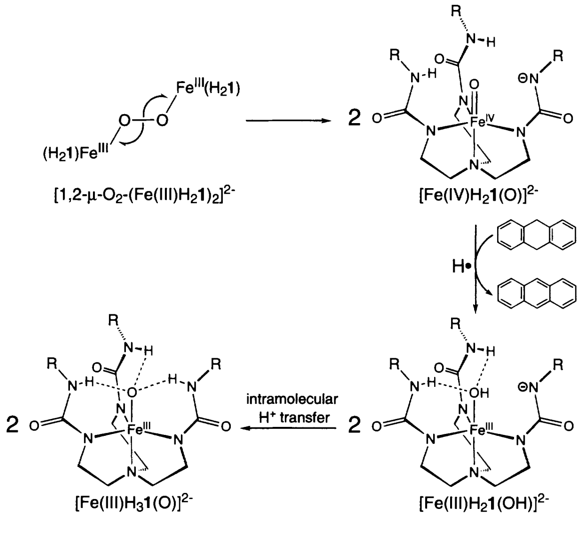

Fig. 2. Proposed mechanism for the formation of $[Fe(III)H_3\mathbf{1}(O)]^{2-}$ in the presence of 9,10-dihydroanthracene.

and structural measurements show that Fe(IV)-oxo porphyrin complexes in proteins also have shorter Fe–O$_{oxo}$ bond lengths (*4*, *5*, *30*, *31*). For example, Fe–O$_{oxo}$ distances of ~1.65 Å are found from extended x-ray absorption fine structure experiments for heme enzymes and related synthetic porphyrin systems with oxoiron(IV) centers.

We also synthesized the related Fe(II)–OH complex [Fe(II)H$_3$**1**(OH)]$^{2-}$ (*24*) by the route shown in Fig. 1. K$_2$[Fe(III)H$_3$**1**(O)] and K$_2$[Fe(II)H$_3$**1**(OH)] have the same charge-to-mass ratio and crystallize in the monoclinic space group $P2_1/n$, with unit cell parameters that differ by <2%. However, large differences are observed in the iron-ligand bond lengths and angles for [Fe(III)H$_3$**1**(O)]$^{2-}$ and [Fe(II)H$_3$**1**(OH)]$^{2-}$ that are consistent with their respective Fe(III)–O and Fe(II)–OH centers. In [Fe(II)H$_3$**1**(OH)]$^{2-}$, the average Fe1–O$_{hydroxo}$ and Fe1–N$_{urea}$ distances, 2.048 ± 0.002 and 2.103 ± 0.002 Å, respectively, are significantly longer than those found in [Fe(III)H$_3$**1**(O)]$^{2-}$. Furthermore, a monomeric Fe(III)–OH complex with a similar H-bonding cavity as in [Fe(III)H$_3$**1**(O)]$^{2-}$ has been reported recently (*22*). As expected, this ferric hydroxo complex has a longer Fe–O$_{hydroxo}$ bond length (1.876 ± 0.002 Å) than the Fe(III)–O$_{oxo}$ bonds in [Fe(III)H$_3$**1-a**(O)]$^{2-}$ and [Fe(III)H$_3$**1-b**(O)]$^{2-}$.

The H-bonding cavity that surrounds the Fe(III)–O$_{oxo}$ unit in [Fe(III)H$_3$**1**(O)]$^{2-}$ is formed by the urea groups of the [H$_3$**1**]$^{3-}$ ligand. The molecular structures of [Fe(III)H$_3$**1-a**(O)]$^{2-}$ and [Fe(III)H$_3$**1-b**(O)]$^{2-}$ show that the three NH groups are directed toward the oxo oxygen. Intramolecular H-bonds between the oxo oxygen and the NH groups are suggested by the observed O$_{oxo}$···N$_{urea}$ distances. For example, in [Fe(III)H$_3$**1-a**(O)]$^{2-}$, these distances are 2.732 ± 0.005 Å for O1a···N3a; 2.702 ± 0.006 Å for O1a···N5a; and 2.686 ± 0.007 Å for O1a···N7a (*32*, *33*). This description of intramolecular H-bonding in [Fe(III)H$_3$**1**(O)]$^{2-}$ is consistent with solid state FTIR studies that show one broad peak for the ν(NH) signals centered at 3130 cm^{-1}. Preliminary ab initio calculations further support the assignment of an Fe(III)–O unit being surrounded by a H-bonding cavity (*34*). The optimized structure reveals that the urea nitrogens N3, N5, and N7 are protonated (N$_{urea}$–H distance of 1.06 Å) with each urea hydrogen positioned 1.57 Å from the oxo ligand and a N–H···O angle of 165°. The calculated charges on the urea hydrogens and oxo oxygen are +0.46 and −1.30, showing that the [H$_3$**1**]$^{3-}$ ligand produces a positively charged cavity around the Fe(III)–O unit. This cavity effect is illustrated by the electron density surface in Fig. 3. The calculation also predicts an Fe–O single bond in [Fe(III)H$_3$**1**(O)]$^{2-}$, which shows that multiple bonding is not always necessary to stabilize M—O units (*35*, *36*).

The Mössbauer spectrum of a powder sample of [Fe(III)H$_3$**1**(O)]$^{2-}$ at 4.2 K exhibits a paramagnetic six-line pattern, whereas a distinctly different paramagnetic six-line pattern is observed for the Mössbauer spectrum of [Fe(III)H$_3$**1**(OH)]$^{1-}$ at 4.2 K. The spectra of both complexes collapse to quadrupole doublets at 77 K with Mössbauer parameters of $\delta = 0.30$ and $\Delta E_Q = 0.71$ mm/s for [Fe(III)H$_3$**1** (O)]$^{2-}$ and $\delta = 0.32$ and $\Delta E_Q = 0.92$ mm/s for [Fe(III)H$_3$**1** (OH)]$^{1-}$. These values fall within the range of the parameters of known high-spin Fe(III) heme and nonheme complexes (*37*, *38*). [Fe(III)H$_3$**1**(O)]$^{2-}$ in DMA displays an axial electron paramagnetic resonance (EPR) spectrum with spectroscopic splitting parameter (g) values of 5.5 and 1.98, indicating a rhombic splitting parameter (E/D) of zero. The spectrum originates from the ±1/2 doublet of the $S = 5/2$ multiplet and quantifies to 100% of the iron in the sample. The temperature dependence of the EPR signal indicates that the axial zero-field splitting parameter is $D = -1$ cm^{-1}; thus, the EPR spectrum is from the second excited doublet. The spectrum of [Fe(III)H$_3$**1**(OH)]$^{1-}$ is more complicated with features at $g = 8.9$, 1.3 and $g = 5.3$, 3.4. These two set of resonances originate from the first (±3/2) and second (±1/2) excited doublets, respectively, of an $S = 5/2$ center with $E/D = 0.17$; thus, [Fe(III)H$_3$**1** (OH)]$^{1-}$ has a substantially more distorted ligand geometry.

Stable monomeric oxometal complexes having greater than four d electrons are rare (*1*). The only structurally characterized examples are Mayer's d^6 oxorhenium(I) complex (*39*) and the d^5 oxoiron(III) complex, [Fe(III)H$_3$**1**(O)]$^{2-}$, reported here. The synthesis and properties of [Fe(III)H$_3$**1**(O)]$^{2-}$ and [Fe(III)H$_3$**1**(OH)]$^{1-}$ resemble those found for [Mn(III)H$_3$**1**(O)]$^{2-}$ and [Mn(III)H$_3$**1** (OH)]$^{1-}$ (*17*). The similarity between these sets of iron and manganese complexes emphasizes the importance of the microenvironment created by the H-bonding cavity of [H$_3$**1**]$^{3-}$ in regulating chemistry. The success in isolating systems like [Fe(III)H$_3$**1**(O)]$^{2-}$ allows for continued structure-function investigations of the role that noncovalent interactions have in metal ion reactivity.

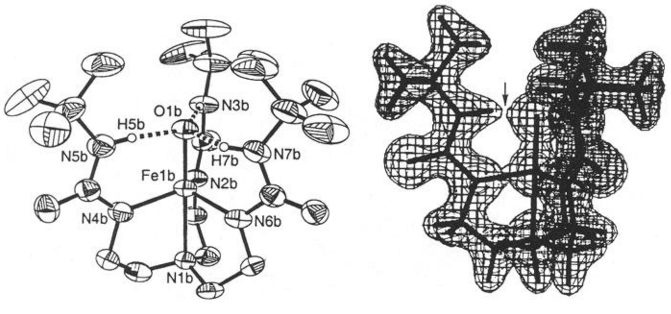

Fig. 3. Thermal ellipsoid diagram of [Fe(III) H$_3$**1-b**(O)]$^{2-}$ (**left**) and an electron density surface derived from ab initio calculations (**right**). The electron density surface was made with the program Titan. The arrow highlights the distortion in the density surface, which is indicative of intramolecular H-bonding between the urea scaffolds of the cavity and the oxo ligand. For clarity, only one H-bonding interaction is shown. The ellipsoids are drawn at the 50% probability level, and only the urea hydrogens are shown. Only one of the disordered fragments of the arm containing N2b is shown. Selected bond lengths (Å) and angles (°) for [Fe(III)H$_3$**1-b**(O)]$^{2-}$ and [Fe(III)H$_3$**1-a**(O)]$^{2-}$: Fe1b–O1b, 1.813 ± 0.003 and 1.813 ± 0.003; Fe1b–N1b, 2.271 ± 0.004 and 2.280 ± 0.004; Fe1b–N2b, 2.030 ± 0.004 and 2.036 ± 0.004; Fe1b–N4b, 2.060 ± 0.004 and 2.070 ± 0.005; Fe1b–N6b, 2.082 ± 0.004 and 2.062 ± 0.005; O1b–Fe1b–N1b, 177.5 ± 0.2 and 177.9 ± 0.2; N2b–Fe1b–N4b, 120.1 ± 0.2 and 117.7 ± 0.2; N2b–Mn1b–N6b, 119.5 ± 0.2 and 121.6 ± 0.2; N4b–Fe1b–N6, 109.1 ± 0.2 and 109.2 ± 0.2.

References and Notes

1. R. H. Holm, *Chem. Rev.* **87**, 1401 (1987).
2. M. Sono *et al.*, *Chem. Rev.* **96**, 2841 (1996).
3. E. I. Solomon *et al.*, *Chem. Rev.* **100**, 235 (2000).
4. V. Fülöp *et al.*, *Structure* **2**, 201 (1994).
5. I. Schlichting *et al.*, *Science* **287**, 1615 (2000).
6. A. L. Balch *et al.*, *J. Am. Chem. Soc.* **107**, 3002 (1985), and references therein.
7. S. J. Lange, H. Miyake, L. Que Jr., *J. Am. Chem. Soc.* **121**, 6330 (1999), and references therein.
8. S. Mukerjee, A. Stassinopoulos, J. P. Caradonna, *J. Am. Chem. Soc.* **119**, 8097 (1997).
9. D. M. Kurtz, *Chem. Rev.* **90**, 585 (1990), and references therein.
10. B. A. Springer *et al.*, *Chem. Rev.* **94**, 699 (1994).
11. Y. Lu and J. S. Valentine, *Curr. Opin. Struct. Biol.* **7**, 495 (1997).
12. M. F. Perutz *et al.*, *Acc. Chem. Res.* **20**, 309 (1987).
13. W. N. Lipscomb and N. Sträter, *Chem. Rev.* **96**, 2375 (1996).
14. M. Mukai *et al.*, *J. Am. Chem. Soc.* **119**, 1758 (1997).
15. Y.-D. Wu *et al.*, *Inorg. Chem.* **31**, 718 (1992).
16. B. S. Hammes, V. G. Young Jr., A. S. Borovik, *Angew. Chem. Int. Ed. Engl.* **38**, 666 (1999).
17. Z. Shirin *et al.*, *J. Am. Chem. Soc.* **122**, 1836 (2000).
18. For examples of the use of H-bonds in metal complexes, see M. Momenteau and C. A. Reed [*Chem. Rev.* **94**, 659 (1994)] and references (*19*–*22*).
19. J. P. Collman and L. Fu, *Acc. Chem. Res.* **32**, 455 (1999).
20. J. E. Kickham, S. J. Loeb, S. L. Murphy, *J. Am. Chem. Soc.* **115**, 7031 (1993).
21. N. Kitajima *et al.*, *J. Am. Chem. Soc.* **116**, 11596 (1994).
22. S. Ogo *et al.*, *Angew. Chem. Int. Ed. Engl.* **37**, 2102 (1998).
23. The [FeO$_4$]$^{2-}$ anion is the only other monomeric oxoiron complex that has been structurally characterized by XRD. The oxo groups in this complex are derived from sources other than O$_2$; see R. H. Herber and D. Johnson, *Inorg. Chem.* **18**, 2787 (1979), and references therein.
24. Synthetic details and characterization of all previously unknown compounds are given in supplementary information, available at www.sciencemag.org/feature/data/1051842.shl.
25. Bond dissociation energies (BDE): C–H in 9,10-dihydroanthracene is 78 kcal/mol (*26*); N–H in urea is 110 kcal/mol (*27*).

26. F. G. Bordwell *et al.*, *J. Am. Chem. Soc.* **113**, 9790 (1991).
27. F. G. Bordwell, J. A. Harrelson Jr., T.-Y. Lynch, *J. Org. Chem.* **55**, 3337 (1990).
28. In $[\mathrm{Fe(III)H_3}\mathbf{1}\text{-}\mathbf{b}\mathrm{(O)}]^{2-}$, one urea arm of the cavity is disordered. All atoms beyond C4b were split into two fragments and refined with restraints. The refinement led to a 0.48:0.52 ratio in occupancy.
29. M. L. Hopper, E. O. Schlemper, R. K. Murmann, *Acta Crystallogr.* **B32**, 2237 (1982).
30. J. E. Penner-Hahn *et al.*, *J. Am. Chem. Soc.* **108**, 7819 (1986).
31. L. A. Anderson and J. H. Dawson, *Struct. Bonding* **74**, 1 (1991).
32. The O···N distances in $[\mathrm{Fe(III)H_3}\mathbf{1b}\mathrm{(O)}]^{2-}$ are as follows: O1b···N3b, 2.732 ± 0.005 Å; O1b···N5b, 2.702 ± 0.006 Å; and O1b···N7b, 2.686 ± 0.007 Å.
33. The O···N distances in $[\mathrm{Fe(II)H_3}\mathbf{1a}\mathrm{(OH)}]^{2-}$ and $[\mathrm{Fe(II)H_3}\mathbf{1b}\mathrm{(OH)}]^{2-}$ are also < 2.900 Å.
34. The geometry of $[\mathrm{Fe(III)H_3}\mathbf{1a}\mathrm{(O)}]^{2-}$ was optimized at the UHF/3-21G* level with Gaussian 98 and assumed C_3 symmetry. The positions of the iron, oxo, and urea nitrogens and hydrogens were relaxed during optimization, whereas those of the other atoms were fixed according to the x-ray structure. The calculated iron-ligand bond distances (Fe1–O1, 1.83; Fe1–N2, 2.27; and Fe1–$\mathrm{N_{urea}}$, 2.03 Å) are similar to those found by XRD methods.
35. R. J. Morris and G. S. Girolomi, *Polyhedron* **7**, 2001 (1988).
36. For a discussion on multiple bonding in C_3 symmetric oxometal complexes, see J. M. Mayer, D. L. Thorn, and T. H. Tulip [*J. Am. Chem. Soc.* **107**, 7454 (1985)].
37. P. G. Debrunner, in *Iron Porphyrins Part III*, A. B. P. Lever and H. B. Gray, Eds. (VCH, Wenheim, Germany, 1989), pp. 139–234.
38. L. Que Jr. and A. E. True, in *Progress in Inorganic Chemistry*, S. J. Lippard, Ed. (Wiley, New York, 1990), vol. 38, pp. 97–200.
39. E. Spaltenstein, R. R. Conry, S. C. Critchlow, J. M. Mayer, *J. Am. Chem. Soc.* **111**, 8741 (1989).
40. We thank the NIH (GM50781 to A.S.B. and GM49970 to M.P.H), ONR-DURIP (9810448 to A. S. B.), E. Münck for use of his Mössbauer spectrometer, and D. Benson, E. Maatta, and R. Schowen for helpful suggestions on the manuscript. Supplementary information available includes the synthetic procedures for all previously unknown compounds and tables and figures for x-ray structural data of $\mathrm{K_2[Fe(II)H_3}\mathbf{1}\mathrm{(OH)]\cdot 4DMA}$ and $\mathrm{K_2[Fe(III)H_3}\mathbf{1}\mathrm{(O)]4DMA}$.

2 May 2000; accepted 20 June 2000

Folds on Europa: Implications for Crustal Cycling and Accommodation of Extension

Louise M. Prockter[1] and Robert T. Pappalardo[2]

Regional-scale undulations with associated small-scale secondary structures are inferred to be folds on Jupiter's moon Europa. Formation is consistent with stresses from tidal deformation, potentially triggering compressional instability of a region of locally high thermal gradient. Folds may compensate for extension elsewhere on Europa and then relax away over time.

Since 1979 when the two Voyager spacecraft began their survey of the outer solar system's icy satellites, abundant extensional tectonic structures but only tentative examples of compressional structures have been identified (*1–3*). Suggested explanations for this conundrum include expansion during freezing of ice I, differential cooling of surface and interior, and displacement of high-density ice polymorphs during differentiation of the largest satellites; however, these mechanisms can account for at most a few percent areal expansion (*1*, *4*, *5*). Early Galileo spacecraft observations found examples of extreme extension (tens of percent regionally) on Europa and Ganymede (*6–8*), yet no subduction zones or large-scale compressional features were recognized (*9*). Thus, the problem of compensating icy satellite extension has been compounded.

The most dramatic and extreme examples of extension on any icy satellite are Europa's dark and gray bands, sites of complete separation of the icy lithosphere above a mobile substrate that has moved up from below to fill the newly created gap (*3*, *10–12*). Morphologic features identified in high-resolution images suggest that the process is in many ways analogous to terrestrial oceanic rifting and spreading (*12*), though corresponding subduction zones are absent.

Morphologic evidence for a series of undulations is found in the region of Astypalaea Linea, a smooth, dark band imaged by Galileo at 43 m/pixel (Fig. 1) (*13*). Astypalaea is inferred to have formed through strike-slip and oblique opening in response to tidally induced stresses (*14*, *15*). The high-resolution Galileo images reveal subtle shading variations crossing Astypalaea Linea almost perpendicular to its trend (Fig. 1A). When a low-pass filter is applied to the image mosaic (*16*), a series of anticlines (fold crests) and synclines (fold troughs) becomes apparent, with wavelength ~25 km (Fig. 1B). These are most evident within the smooth material of Astypalaea itself, but continue into the ridged plains surrounding the band; thus, the folds postdate the band and the adjacent ridged plains.

Corroborative evidence for the fold interpretation comes from small-scale structures along the inferred anticline and syncline axes. In general, anticline crests are sites of local tensile stress whereas synclines are sites of compressive stress, and corresponding small-scale structures are expected. Three discrete sets of small-scale fractures (troughs) are observed to cut across Astypalaea Linea, many continuing into the surrounding terrain (Figs. 1C and 2). These fractures occur along the crests of the regional-scale anticlines inferred from shading. The troughs are somewhat anastomosing and less linear than typical Europan troughs and are unusual in that they occur in fracture sets.

We also find four well-separated sets of small-scale subparallel ridges (Fig. 2). The ridges are short (~2 to 3 km), narrow (~0.5 km), and quite irregular in planform. These small ridges occur within the inferred synclinal lows, trending subparallel to the fold axes (Fig. 1). The ridges are inferred to be compressional structures (folds and/or thrust blocks) formed within regional-scale synclines. They are found within Astypalaea but not within the surrounding ridged plains, perhaps because the band material is more easily deformable or because the structures are more easily identified within the smooth band material.

The identification of folds is significant to the geological history and resurfacing style of Europa, because we can now begin to understand how the satellite's ubiquitous extension (specifically, band formation) is compensated by compression. In the Astypalaea region, we estimate that crest-to-trough fold height is at least ~100 m (in order to be perceived) but no more than ~1 km [which is the greatest topography observed on Europa (*17*)]. If the folds have a perfect sinusoidal form and volume was conserved during folding, this height range implies a local compressional strain ε between −0.004% and −0.4%; if the fold limbs are straight in the manner of kink folds, then ε can be up to −0.9% (*18*). Some degree of extensional strain has been accommodated by regional-scale folding of the lithosphere, but this relatively small degree of compressional strain is not sufficient to accommodate Europa's abundant extensional deformation.

Several lines of evidence suggest that Europa's shell has been tidally deformed in response to a combination of diurnal and nonsynchronous rotation stresses, which predicts specific surface patterns of compressive and tensile stress that shift on the time scale of each cycle (*19–22*). The long-period nonsynchronous rotation stress in the Astypalaea area builds by ~80 kPa per degree of rotation (a period of $>10^4$ years if occurring today) (*19*, *21*). The

---

[1] Applied Physics Laboratory, Johns Hopkins University, MS 7-366, 11100 Johns Hopkins Road, Laurel, MD 20723, USA. [2] Brown University, Department of Geological Sciences, Box 1846, Providence, RI 02912, USA.

E-mail: louise.prockter@jhuapl.edu; robert_pappalardo@brown.edu